Supporting information.

Understanding the Performance Limiting Factors of Cs$_2$AgBiBr$_6$ Double-Perovskite Solar Cells

Giulia Longo,[‡†] Suhas Mahesh,[†] Leonardo R. V. Buizza,[†] Adam D. Wright,[†] Alexandra J. Ramadan,[†] Mojtaba Abdi-Jalebi, [ǂ] Pabitra K. Nayak,[#] Laura M. Herz,[†] Henry J. Snaith[†]

‡ Department of Mathematics, Physics and Electrical Engineering, Northumbria University, Ellison place, Newcastle upon Tyne, NE18ST, United Kingdom

† Clarendon Laboratory, Department of Physics, University of Oxford, Parks Road, Oxford, OX13PU, United Kingdom

Institute for Material Discovery, University College London, Torrington Place, London, WC1E 7JE, United Kingdom

ǂ Cavendish Laboratory, Department of Physics, University of Cambridge, JJ Thomson Avenue, Cambridge CB3 0HE, United Kingdom

#TIFR Centre for Interdisciplinary Sciences, Tata Institute of Fundamental Research, Hyderabad, 500107, India

Cs$_2$AgBiBr$_6$ thin film preparation for characterization. The double-perovskite thin films studied in this work were all prepared through sequential vapour deposition. In a vacuum-sealed chamber, AgBr (99% Fluka), BiBr$_3$ (≥98% Sigma Aldrich) and CsBr (99.9% Sigma

Aldrich) were placed in separate crucibles and sequentially thermally evaporated onto the substrates. In particular, the standard procedure we optimized evaporated 90 nm of AgBr, 120 nm of $BiBr_3$ and 150 nm of CsBr to obtain 300 nm of $Cs_2AgBiBr_6$. This basic stack was repeated the necessary number of times to achieve the desired total film thickness. To achieve thicknesses that are not multiples of 300 nm (like the 750 nm reported in the text), we ran the last evaporation cycle depositing half of each precursor thickness, keeping always the same precursors ratio (1:1.3:1.6 $AgBr:BiBr_3:CsBr$). After the deposition of the desired thickness, we annealed the samples on a hotplate in air at 250 ºC for 30 minutes. The post-deposition annealing temperature and time were optimised to deliver maximum solar cell performance.

Solar cell preparation. FTO or ITO coated glasses were cleaned by sequential sonication in soap, water, acetone and isopropanol. After being dried with a N_2 gun, the substrates were further cleaned by O_2 plasma for 10 minutes. Titanium isopropoxide (140 μl in 1 ml of EtOH) was added to 1 ml of acidic EtOH (10 μl of HCl 2M in 1 ml EtOH), and deposited on the FTO substrates by spincoating at 2000 rpm for 45 sec with 2000 rpm/sec acceleration. Following this, the films were annealed at 150°C for 15 min and 500°C for 30 min. SnO_2 layers were prepared by spincoating at 3000 rpm (200 rpm/sec) for 30 sec of a solution of $SnCl_4·5H_2O$ in isopropanol (17.5 mg/ml) on top of the FTO or ITO coated glasses. The so-prepared films were annealed at 100°C for 10 min followed by an annealing at 180°C for 30 min. The SnO_2 and TiO_2 films were placed in the vacuum chamber, and the $Cs_2AgBiBr_6$ film was deposited as previously presented. The hole transport material (Spiro-OMeTAD, Lumtec) was dissolved in chlorobenzene (85 mg/ml) and doped with 20 μl of LiTFSI (500 mg/ml in BuOH) and 30 μl of tert-butylpyridine. The solution was then deposited on the active layer by spincoating in air at 2000 rpm (2000 rpm/sec) for 45 sec. The devices were then left overnight in a desiccator in air atmosphere, and then completed by the evaporation of 100 nm silver contacts. All the

characterizations were performed in air. Semi-transparent devices were fabricated by substituting the silver by 20 nm of gold, and using a 435 nm thick double-perovskite absorber.

SPV sample preparation. For the surface photovoltage measurements, FTO substrates were used. Different hole and electron transport materials were deposited on the FTO through spincoating in air: TiO_2 (as previously described), SnO_2 (as described above), PCBM (10 mg/ml in chlorobenzene, 2000 rpm 60 sec, 2000 rpm/sec), Spiro-OMeTAD (as previously), P3HT (15 mg/ml in chlorobenzene, 2000 rpm 45 sec, 200 rpm/sec). 300 nm of $Cs_2AgBiBr_6$ was deposited on top of those substrates as well as on bare FTO, and annealed at 250°C for 30 min. In order to avoid transport material degradation, the annealing time for the samples with PCBM, Spiro and P3HT was reduced to 5 min.

XRD measurements. Powder XRD patterns were recorded on a Panalytical X'pert powder diffractometer (equipped with Cu Kα1 anode X-ray source, and radiation; $\lambda = 1.5405$ Å). The samples, consisting of a $Cs_2AgBiBr_6$ thin film on a quartz substrate, were rotated during data collection, which was done at room temperature and normal indoor lighting conditions

Absorption, PL and PLE measurements. Absorption spectra of $Cs_2AgBiBr_6$ on glass were measured using a Varian Cary 300 UV-Vis spectrophotometer. Photoluminescence emission and excitation spectra were collected with a spectrofluorimeter (Fluorolog, Horiba), with a 450 W Xenon lamp excitation source and a photomultiplier tube detector. For these measurements, samples on quartz were used.

Photothermal deflection spectroscopy. PDS is a scatter-free surface sensitive absorption measurement capable of measuring several orders of magnitude weaker absorbance than the

band edge absorption. For the measurements, a monochromatic pump light beam is shined on the sample (double-perovskite thin film on quartz substrate), which on absorption produces a thermal gradient near the sample surface via non-radiative relaxation induced heating. This results in a refractive index gradient in the area surrounding the sample surface. This refractive index gradient is further enhanced by immersing the sample in an inert liquid FC-72 Fluorinert® (3M Company) which has a high refractive index change per unit change in temperature. A fixed wavelength CW laser probe beam is passed through this refractive index gradient producing a deflection proportional to the absorbed light at that particular wavelength, which is detected by a photo-diode and lock-in amplifier combination. Scanning through different wavelengths provide the complete absorption spectra.

Optical Modelling. We modelled the optical response of the stack using the generalised transfer matrix method.[1] All calculations were performed in Python using the NumPy and SciPy libraries. Transfer matrix calculations take the complex refractive index spectrum and thickness for each layer as input. The stack used was Glass/ITO (200 nm)/SnO_2 (20 nm)/$Cs_2AgBiBr_6$ (435 nm)/Spiro-OMeTAD (200 nm)/ Au (20 nm). The calculation provides us with the intensity of light at any cross-section of the stack, which can be used to calculate the generation within any desired volume of the solar cell. We assume that with diffusion length of de(h), all electrons (holes) generated within a distance de(h) of the electron (hole) transporting layer are collected. The cell current is determined by the smaller of the electron and hole currents. The stack used was (Au(20 nm)/Spiro-OMeTAD(200 nm)/Perovskite(435 nm)/SnO2(20 nm)/ITO(200 nm)/Glass). The transfer matrix method was used to calculate, for each wavelength, the fraction of photons absorbed within a distance de(h) from the electron (hole) transporting layer. We make the assumption that there is no current loss at the interfaces. Then, the smaller of the two calculated photon fractions is, by definition, the external quantum

efficiency of the cell at each wavelength. We then obtained the best fit for the measured EQE by varying de and dh using the Newton-Raphson method implemented in the library Scipy.

Optical-Pump Terahertz-Probe Spectroscopy:

OPTP is a standard non-contact characterization technique that provides information about local charge-carrier mobility at THz frequencies. Terahertz radiation probes the dielectric response of a medium in the low-frequency range, allowing the examination of charge-carriers present, as they modify the conductivity at THz frequencies. OPTP spectroscopy offers the possibility to time-resolve changes in the electric field amplitude ($\Delta T/T$) of a single-cycle terahertz pulse transmitted to a sample as a function of time delay after optical excitation. The measured transient signal allows us to evaluate the change in the photoconductivity (ΔS) of photoactive materials, and from there, it is possible to calculate the sum of electron and hole mobilities for the material ($\Sigma\mu$) from the initial $\Delta T/T$ values. It is important to note that the calculated effective charge-carrier mobility is always an and only in the case of full conversion of photons to free charges our value reflects the true mobility. Additionally, the calculated value of μ arises from changes in photoconductivity due to both electrons and holes, meaning we calculate an overall sum mobility.

An amplified laser system (Spectra Physics, MaiTai – Ascend – Spitfire), with a 5 kHz repetition rate, centre wavelength of 800 nm and pulse duration of 35 fs was used to generate THz radiation via the inverse-spin Hall effect from a spintronic emitter, as described elsewhere.[2] The THz probe was focused onto the sample and detected via free-space electro-optical sampling in a ZnTe(110) crystal of thickness 200 μm. A 400 nm pump pulse was generated using a Beta Barium Borate (BBO) crystal. Transient decays were measured by recording the change in peak THz amplitude transmitted as a function of pump-probe delay time. Measurements were carried out under vacuum ($< 10^{-2}$ mbar).

Thin-film samples were excited at 400 nm with an amplified laser with low repetition rate illuminating from the perovskite side of the films. We measured the change in terahertz transmission ($\Delta T/T$) over time. At low fluences ($< 50\ \mu Jcm^{-2}$) there is a linear relationship between the charge-carrier mobility μ and the change in photoconductivity of the sample ΔS:

$$\mu = \frac{\Delta S\ A_{eff}}{Ne}.$$

<div align="right">S1</div>

The change in photoconductivity can in turn be related to the fractional change in terahertz transmission using a standard formula for thin-film samples:[3]

$$\Delta S = -\epsilon_0 c(n_A + n_B)\left(\frac{\Delta T(t=0)}{T}\right).$$

<div align="right">S2</div>

We can also calculate the number of photoexcited charge carriers using:

$$N = \phi \frac{E\ \lambda}{h\ c}\left(1 - R_{pump}(\lambda)\right)\left(1 - T_{pump}(\lambda)\right),$$

<div align="right">S3</div>

where ϕ is the free-charges to absorbed photons branching ratio.

We can combine equations S3, S2 and S1, to calculate the effective charge-carrier mobility as:

$$\phi\mu = -\epsilon_0 c(n_A + n_B)\frac{A_{eff}hc}{Ee\lambda\left(1 - R_{pump}(\lambda)\right)\left(1 - T_{pump}(\lambda)\right)}\left(\frac{\Delta T(t=0)}{T}\right)$$

<div align="right">S4</div>

The charge-carrier diffusion length can be calculated by converting the mobility into diffusion co-efficient, D, following the Einstein relationship (Equation S5) and applying the relationship in Equation S6

$$D = \frac{k_B T}{q}\mu$$

<div align="right">S5</div>

$$L_D = \sqrt{\frac{D}{R_T(n)}}$$

<div align="right">S6</div>

where T is the temperature, k_B the Boltzmann constant, q the elementary charge and $R_T(n)$ is the charge-carrier recombination rate.

Time-Correlated Single-Photon Counting: The time-resolved PL of a thin-film on quartz (mounted in a He atmosphere) was measured using Time Correlated Single Photon Counting (TCSPC) following excitation by a 400 nm picosecond pulsed diode laser (PicoHarp, LDH-D-C-405M). The resultant PL was collected and coupled into a grating spectrometer (Princeton Instruments, SP-2558), which directed the spectrally dispersed PL onto a photon-counting detector (PDM series from MPD), whose timing was controlled with a PicoHarp300 TCSPC event timer. A laser fluence of 0.24 μJ cm^{-2} was used. The PL transient was measured at 638 nm, which was the wavelength of peak PL intensity in the PL spectrum measured by this system. The PL decay trace was fitted by a monoexponential function between 0 and 1.2 ns, the time window of the OPTP measurements, obtaining a PL lifetime of of τ = 1.3 ns. This function had the form $I = I_0\ exp(-t/\tau)$, where τ is the PL lifetime representative of the charge-carrier recombination rate occurring during this time window. To obtain a lifetime representing the full transient, we also fitted a stretched exponential function $I = I_0\ exp(-(t/\tau_c)^\beta)$, where β is the distribution coefficient and τ_c is the time taken for the PL intensity to drop to I_0/e. The obtained mean lifetime is τ_{av} = 10 ns. Such stretched exponential functions have been used to phenomenologically account for the presence of a local distribution of monoexponential decay rates, whose average lifetime is given by $\tau_{av} = (\tau_c/\beta)\ \Gamma(1/\beta)$, where Γ is the gamma function.[4,5]. Following the convention of Richter et al.,[6] we double the fitted lifetime in order to extract our charge-carrier recombination rate, so that $k_1 = 1/2\tau_{meas}$, giving values for k_1 of 5–38.5*10^7 s^{-1}.

Kelvin Probe and Surface Photovoltage. Kelvin probe is a not invasive technique that permits the evaluation of the work-function of a material through capacitance measurements between the sample and a reference (an oscillating tip) with known work-function. The work principle

is schematically represented in Figure S6. With no connection, the two materials are electrically neutral, and they share the same local vacuum level Figure S6a). When the circuit is closed, electrons flow from the material with lower work-function to the higher one, creating an electric field between the two plates of the capacitor (sample surface and oscillating tip) and aligning the Fermi levels (Figure S6b). The local vacuum level drop, which is the difference between the two work-function, is called contact potential difference (CPD). Its direct evaluation is quite challenging, so, in the Kelvin probe technique, a null-method is used for the evaluation of the CPD. When an external bias with value V = -CPD is applied, the Fermi levels are not aligned anymore, and the capacitor is discharged (Figure S6c). Then, the CPD is evaluated looking for the applied voltage that discharge the capacitor. The surface photovoltage (SPV) is the measurement of the change of the CPD when the sample is illuminated, and is calculated as the difference between the CPD under light and the CPD in dark. The potential of the surface, is usually different from the bulk value. This is due to the presence of surface states (due to defects, dangling bonds or adsorbed molecules), and it causes a bending in the potential and in the local vacuum level. The region where this potential change occurs is called space charge region (SCR), and the direction of the bending depends on the charge accumulating at the surface. We schematically represent it in Figure S6d for the case of a n-type semiconductor. Upon above band gap photoexcitation, photo-generated electrons will drift away from the band bending region, while holes will move to the surface, reducing the band-bending and resulting in a subsequent reduction in the contact potential difference (Figure S6e).

Ultraviolet photoemission spectroscopy. UPS measurements were performed using a custom built ultrahigh vacuum (UHV) system (base pressure of 10^{-10} mbar) using a helium discharge lamp (21.22 eV). The work-function of the samples was determined using the secondary electron cut-off spectra (SECO) recorded with a 10 V bias applied to the sample to overcome

the analyser work-function and all spectra were recorded at normal emission and room temperature using a hemispherical SPECPhoibos 100 analyzer. The energy resolution of these measurements was 120 meV. The results were fitted with a linear function obtaining a work-function value of 4.94 eV and a valence band maximum of 6.8 ± 0.3 eV. The valence band onset for this material was incredibly shallow and as such there was some ambiguity associated with its fitting. To avoid misreporting the position we have chosen to report the value with a larger error range than typically associated with these measurements (< 0.1 eV).
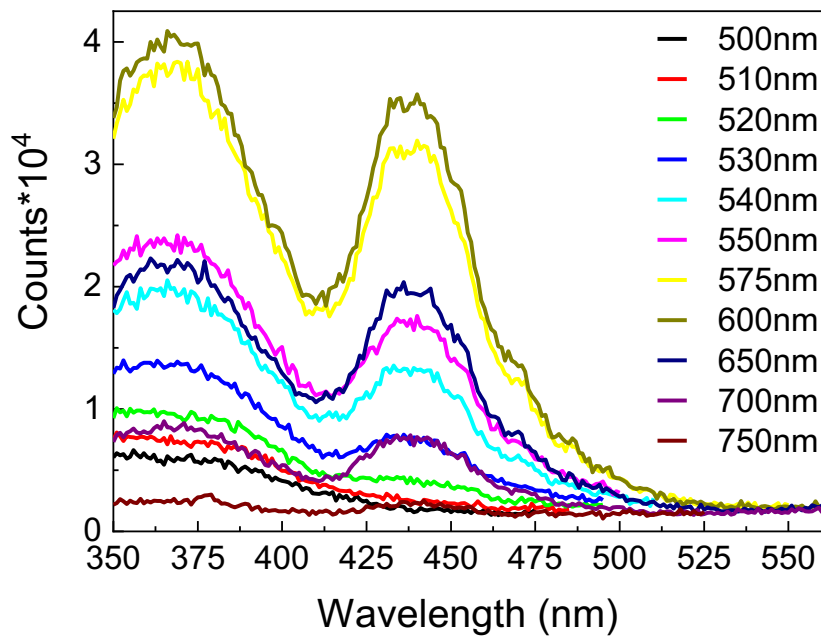
Figure S1 Photoluminescence excitation spectra (PLE) of $Cs_2AgBiBr_6$ thin-film recorded for different emission wavelengths.
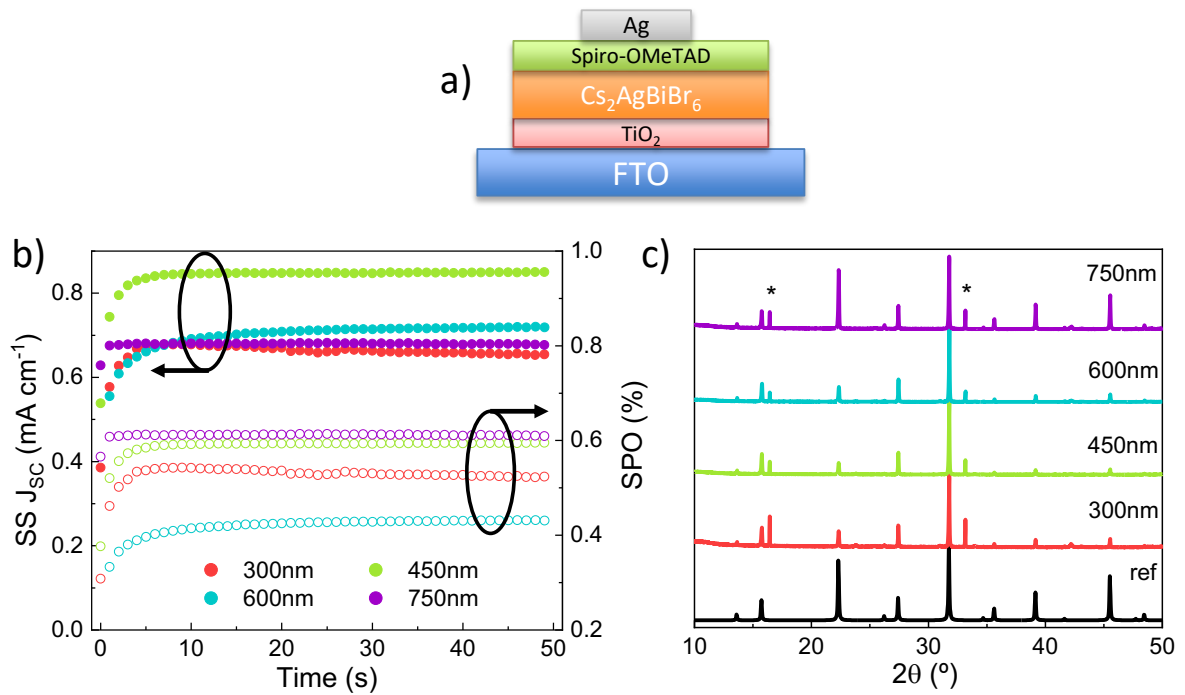
Figure S2 a) Schematic illustration of the solar cell architecture. b) Steady-state Jsc (SS J_{SC}) and steady-state power output (SPO) of the devices with different $Cs_2AgBiBr_6$ thickness. c) XRD patterns of the double-perovskite with different thickness. The peaks marked with a star derive from the quartz substrates.
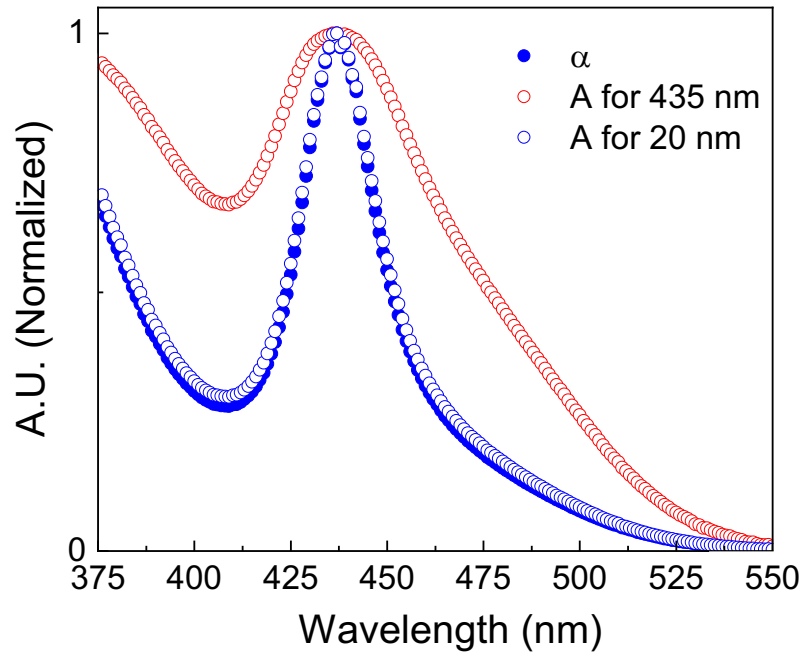
Figure S3 Normalized absorption coefficient (α, blue filled circles), and the calculated absorptance (A) for 435 nm thick (red empty circles) and 20 nm (blue empty circles) thick $Cs_2AgBiBr_6$ films.
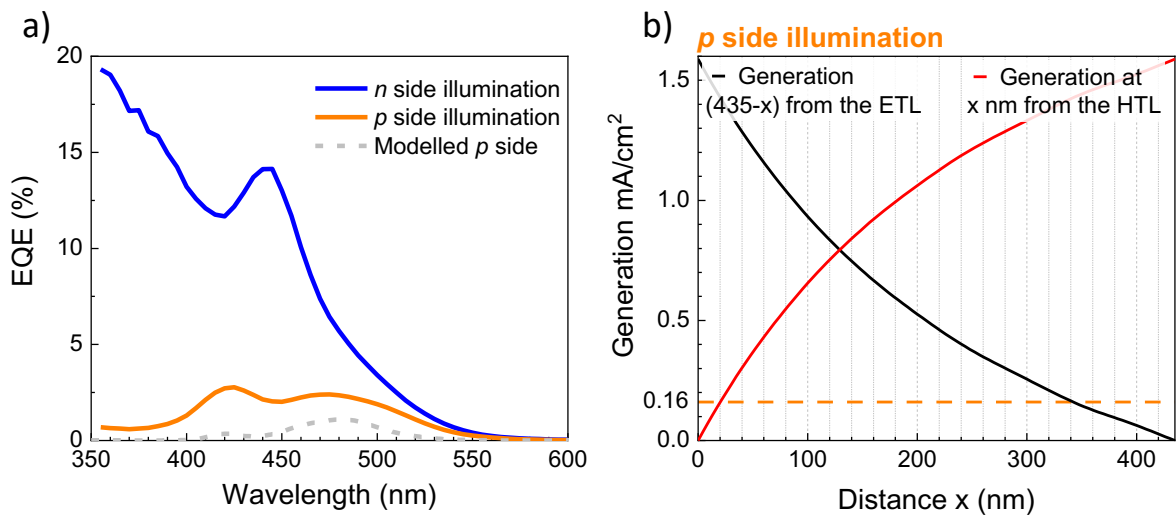

Figure S4 a) EQE measured with illumination from the ITO (blue curve), from the gold (orange curve) and the modelled p-EQE (grey dashed curve). c) Current generation at a distance x from the HTL (red curve) and from a distance 435-x from the ETL (black curve) in the case of p-

side illumination. The dashed orange line indicates the current obtained from the integration of the p-EQE
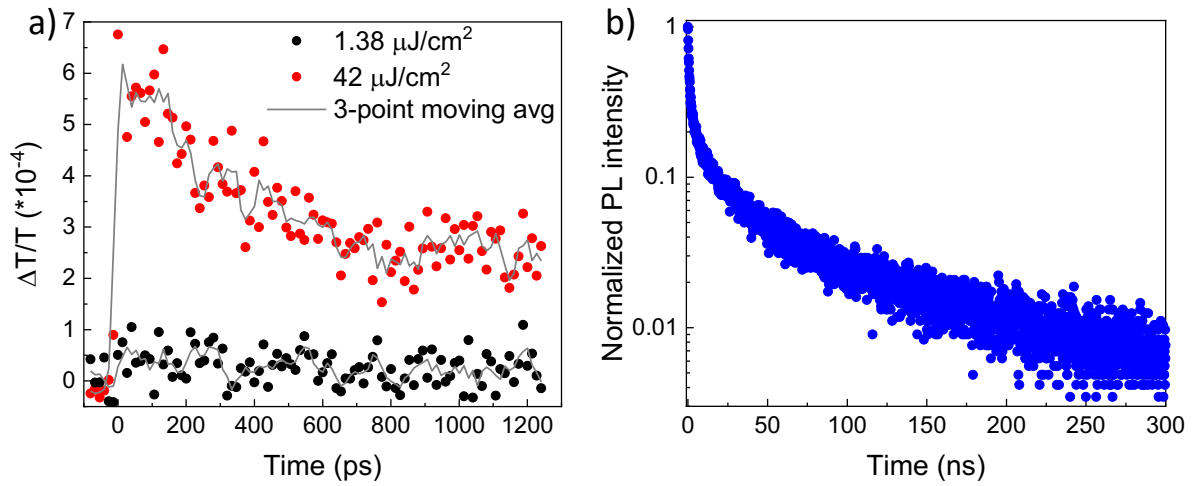

Figure S5 a) Transient OPTP decays and corresponding 3-point moving averages of a $Cs_2AgBiBr_6$ thin-film deposited on z-cut quartz and b) time resolved photoluminescence decay, measured close to the peak PL wavelength with an excitation fluence of 0.24 μJ/cm². In both cases excitation wavelength was 400 nm
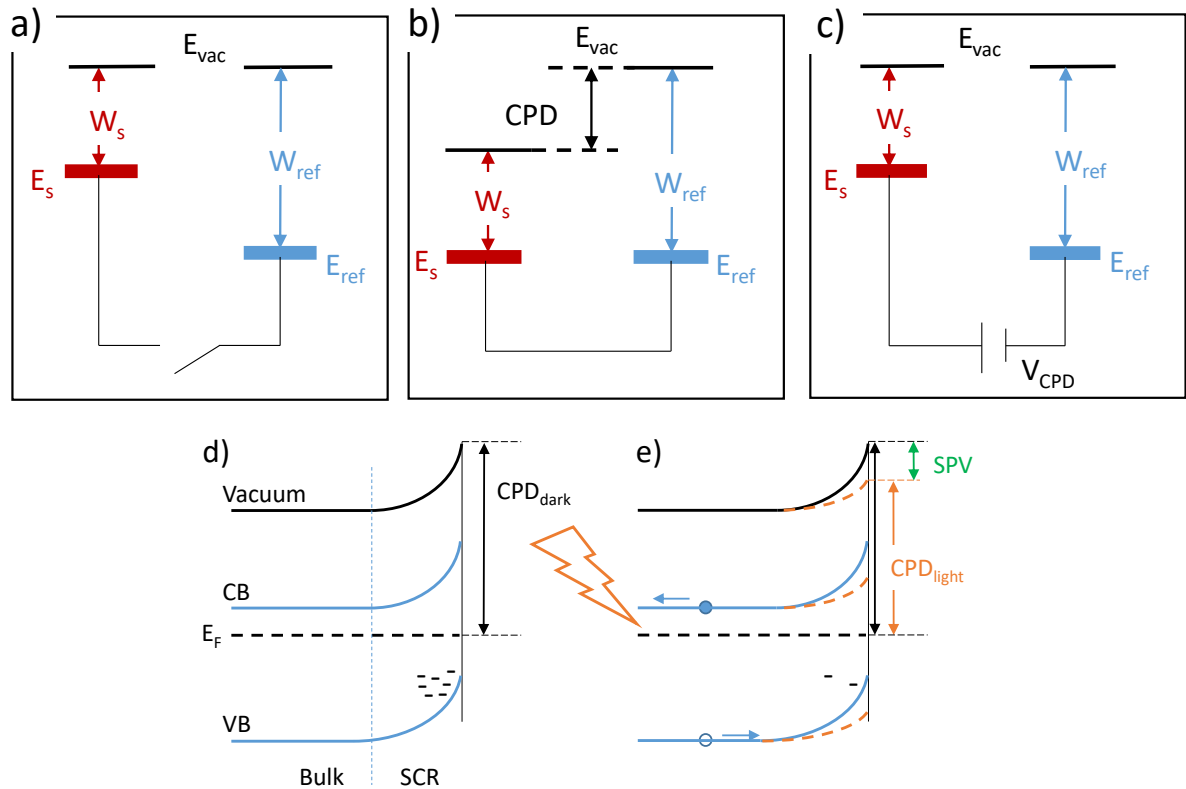
Figure S6 a,b,c) Schematic representation of the working principle of the Kelvin Probe. In the pictures W_s and W_{ref} are the working functions of the sample and the reference (oscillating tip), respectively, E_s and E_{ref} the Fermi levels of the sample and the reference, CPD is the contact potential difference and V_{CPD} is the applied voltage necessary to discharge the capacitor. d) Potential bending at the surface for a n-type semiconductor in dark and e) the reduction of the potential bending upon illumination and the corresponding SPV
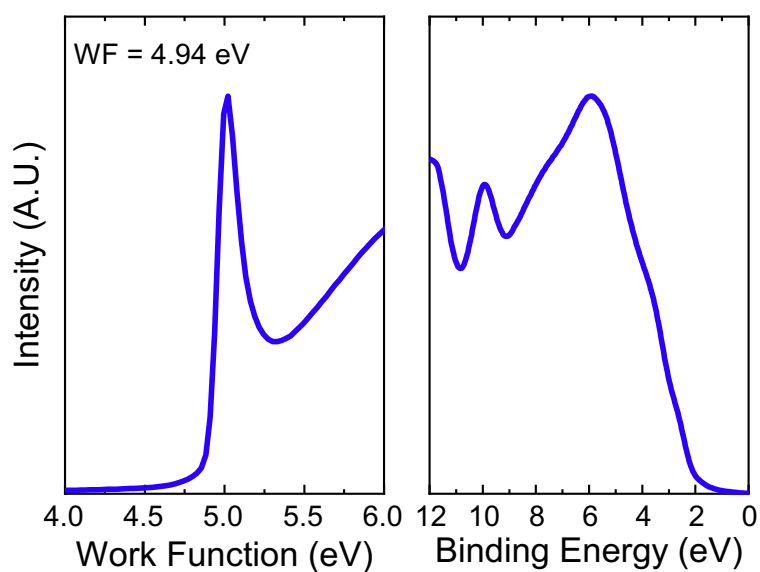
Figure S7 UPS spectroscopy for $Cs_2AgBiBr_6$ thin film deposited on FTO. Left panel shows the secondary electron cut-off (SECO) region from which the work-function (reported in the panel) was calculated. Right panel shows the valence band region.

	300 nm	450 nm	600 nm	750 nm
PCE (%)	0.468	0.686	0.535	0.696
J_{SC} (mA cm^{-1})	0.676	0.896	0.702	0.837
V_{OC} (V)	1.10	1.10	1.05	1.15
FF (%)	62	68	73	71
SPO (%)	0.523	0.595	0.431	0.609
SS J_{SC} (mA cm^{-1})	0.654	0.850	0.719	0.676

Table S1 Figure of merit of the J-V curves, steady-state Jsc and steady-state power output (SPO) of the devices with different $Cs_2AgBiBr_6$ thicknesses

References

1   Centurioni, E. Generalized matrix method for calculation of internal light energy flux in mixed coherent and incoherent multilayers. *Appl. Opt.* **2005**, *44*, 7532-7539.

2   Buizza, L. R. V., Crothers, T. W., Wang, Z., Patel, J. B., Milot, R. L., Snaith, H. J., Johnston, M. B., Herz, L. M. Charge-Carrier Dynamics, Mobilities, and Diffusion Lengths of 2D–3D Hybrid Butylammonium–Cesium–Formamidinium Lead Halide Perovskites. *Advanced Functional Materials* **2019**, *29*, 1902656.

3   Joyce, H. J., Boland, J. L., Davies, C. L., Baig, S. A. & Johnston, M. B. A review of the electrical properties of semiconductor nanowires: insights gained from terahertz conductivity spectroscopy. *Semicond. Sci. Technol.* **2016**, *31*, 103003.

4   Parrott, E. S., Green, T., Milot, R. L., Johnston, M. B., Snaith, H. J.,   Herz, L. M. Interplay of Structural and Optoelectronic Properties in Formamidinium Mixed Tin–Lead Triiodide Perovskites. *Adv. Funct. Mater.* **2018**, *28*, 1802803.

5   Lindsey, C. P. & Patterson, G. D. Detailed comparison of the Williams–Watts and Cole–Davidson functions. *J. Chem. Phys.* **1980**, *73*, 3348-3357.

6   Richter, J. M., Abdi-Jalebi, M., Sadhanala, A., Tabachnyk, M., Rivett, J. P. H., Pazos-Outón, L. M., Gödel, K. C., Price, M, Deschler, F., Friend, R. H., Enhancing photoluminescence yields in lead halide perovskites by photon recycling and light out-coupling. *Nat. Commun.* **2016**, *7*, 13941.